RIGOROUS APPROACH TO CALCULATION OF CAPACITANCE IMAGES OF METALLIC SAMPLES FOR USE IN CAPACITANCE MICROSCOPY

Galyna Safonova[1, 2, *] and Elena D. Vinogradova[1]

[1]Department of Mathematics, Macquarie University, North Ryde, NSW 2109, Australia

[2]Phenomics and Bioinformatics Research Centre, School of Informational Technology Mathematical Sciences, University of South Australia, Mawson Lakes, SA 5095, Australia

Abstract—A high-efficiency rigorous approach for the solution of the two-dimensional Laplace equation with Dirichlet's boundary conditions is developed to tackle electrostatic problems involving metallic cylinders of arbitrarily cross-sections. In this paper, we demonstrate how this novel algorithm can be used to address the problems arising in the capacitance microscopy to provide a higher resolution in studies of micro-cavities and whiskers on the surface of metallic samples. The precise capacitance images of the probe/sample systems are presented.

1. INTRODUCTION

Scanning capacitance microscopy (SCM) is mostly associated with a technique of imaging dopant variations in semiconductor devices (see, for example [1]). SCM is often used to measure implant profiles. Another SCM application is the low-frequency microscopy measurements based on capacitance scanning, used to determine variations in thin, dielectric films with resolution up to 1 nm in thickness and 200 nm laterally [2]. This technique may be used on metallic substrates as well as semiconducting substrates. Omitting the technical details, SCM can be described as a microscopy technique using a narrow probe electrode held just above the surface of a sample to scan the capacitance values across the sample. SCM characterizes the surface of the sample by the change in the electrostatic capacitance

between the surface and the probe and is a useful tool to reconstruct the surface topography of a rough metallic sample based on its capacitance image (dependence of capacitance of the system on a relative angular probe/sample position). Recent developments in the field are described, for example, in [3–6]. Various algorithms have been developed to allow efficient capacitance calculations [7–10]. However, purely numerical algorithms are usually very time consuming and most of them do not provide a guarantee of convergence as the grid size is refined. Analytical algorithms, on the other hand, are usually only capable of providing solutions for a limited number of idealized structures (see, for example [11, 12]).

Therefore, there is a need for a fast and reliable algorithm for calculating capacitance of the systems where high pre-specified accuracy is required. Our algorithm we developed to address this issue is based on method of analytical regularization (MAR). This method has previously been applied successfully in [13, 14] to the integral equations associated with potential and wave scattering problems involving single conductors of the canonical shape (with circular, elliptic or rectangular cross-section). The main idea of MAR is in transforming Fredholm integral equations of the first kind into the well-conditioned and fast converging Fredholm equations of the second kind in a matrix formulation.

In this paper, the above approach is generalized for boundary value problems in potential theory associated with the assembly of arbitrarily profiled charged cylinders. The main steps of the solution of the integral equations for the unknown charge density functions obtained from Laplace's equation are:

- splitting the kernel of an integral equation into a suitable singular part and a smooth remainder;
- implicit analytical inversion of the singular part;
- expansion of the remaining continuously differentiable functions into Fourier series;
- rescaling of the matrix coefficients to obtain Fredholm equations of the second kind.

The existence of the Fredholm alternative for such equations guarantees that the solution of the truncated system of the Fredholm equations of the second kind converges to a solution of the infinite system. The accuracy of the solution will only depend on truncation number and can thus be pre-specified. The details of the method are discussed in Section 2. The second major advantage of our developed algorithm is the short computational time achieved by using the fast Fourier transform for computation of the matrix elements.

The possible applications of our algorithm are not limited by SCM. The method is suitable for solving 2-D electrostatic problems for multiple conductors with no restrictions on system geometry except for the requirement of smooth parameterization of the contours. Such flexibility allows this algorithm to be applied to various problems such as TEM-mode analysis in the different types of homogeneous transmission lines, studies of finite gratings and an ensemble of the conductors above the grounded plane, and advanced analysis of the electrostatic potential distribution in the quadrupole mass-spectrometer. In this paper, we use the flexibility and reliability of our developed method to calculate the capacitance image of the metallic samples, a direct problem associated with SCM. The SCM operation, however, seems to be one of most suitable among many possible applications of our algorithm since it deals with charged conductors/samples of arbitrarily shape and, in addition, the 2D-space electric field may be computed, as mentioned above, with any desired degree of accuracy.

The paper is organized as follows. In Section 2, the mathematical background of the method is described. This approach reduces the initial problem to coupled infinite systems of linear algebraic equations of the second kind. The Fredholm's nature (compactness) of operators in each of the coupled systems provides fast convergence of the truncated finite systems to the exact solution; the accuracy of computations strictly depends on truncation number. With a proper choice of truncation number the calculations may be carried out with any prescribed accuracy.

In Section 3, we employ the geometry of the 2-D capacitance microscope described in [7] for numerical calculations. Initially, as a mean of verification, we consider the elliptic cylinder positioned in the centre of the shield or elevated. Next we use three geometries: rectangular cylinder, four-ray star-shaped cylinder and periodically perforated ("rough") circular cylinder. The capacitance images of all samples are discussed.

In Conclusions, we resume the obtained results and discuss a possibility of further generalization of the method.

2. THEORETICAL BACKGROUND

The method described in this paper may be classified as an analytical-numerical method with generic features of reliability and stability, in contrast to the purely numerical techniques, where it is not possible to guarantee convergence or accuracy when some parameter, such as grid size is increasingly refined. Our algorithm is based on the method of

analytical regularization; details of this method applied to scattering problems for canonical structures are presented in [13, 14].

Generally, our algorithm is developed to tackle the problems with $N - 1$ arbitrarily profiled charged PEC cylinders embedded into a homogeneous dielectric medium with relative permittivity ε, where N is a positive integer exceeding 1. To ensure that the two-dimensional electrostatic potential problem is physically reasonable we consider a case when a finite dielectric medium is bounded by an infinitesimally thin grounded cylindrical shell. This problem is fully described by the Dirichlet boundary value problem for Laplace's equation for the electrostatic potential U,

$$\Delta U = 0 \tag{1}$$

with boundary conditions for the potentials given at the surface boundary L_n $(n = 1, \ldots, N)$ of each of the N cylinders:

$$U|_{L_n} = V_n, \ n = 1, \ldots, N, \tag{2}$$

where $V_N = 0$ for a system with a grounded shield enclosing all other cylinders. To employ the regularization procedure all contours, L_n must be smooth and non-self crossing with a continuous parameterization that is twice differentiable at each point of L_n.

As all conductors are arbitrarily-shaped the classical separation of variables method is not applicable here. We use a more general approach based on an integral representation. Using the superposition principle we seek a solution for the total field potential U as the sum of the single-layer potentials contributed by each cylinder,

$$U(q) = \sum_{j=1}^{N} \int_{L_j} G(|p - q|) Z_j(p) dL_p. \tag{3}$$

Here

$$Z(p) = \frac{dU}{dn}(p)$$

where $d/dn(p)$ denotes a normal derivative at the point p. $Z(p)$ is related to the linear charge distribution $Q(p)$ on the contour L by $Q = \varepsilon Z / 4\pi$ (where ε is a permittivity).

Kernel G of the integral Equation (3) is the two-dimensional free space Green's function,

$$G = -\frac{1}{2\pi} \log(|p - q|), \tag{4}$$

where $|p - q|$ is the distance between points p and q normalized by a largest cylinder radius R_{char}. Applying boundary conditions to

Equation (3) we obtain the coupled system of integral equations for the unknowns Z_j:

$$\sum_{j=1}^{N} \int_{L_j} G_{ij}(|p-q|)Z_j(p)dL_p = V_s(q), \quad s = 1, \ldots, N \qquad (5)$$

where V_s is the potential given on the n-th boundary.

Equation (5) represents first kind Fredholm integral equations that are generally ill-posed. Our algorithm is designed to transform these initial equations into second kind Fredholm equations by analytical means. Numerical truncation methods can then be effectively applied.

First, we need to parametrize each contour L_n,

$$\eta_s(\theta) \equiv (x_s(\theta), y_s(\theta)), \quad (s = 1, \ldots, N), \ \theta \in [-\pi, \pi]$$

and introduce some new notations

$$z_j = l_j(\theta)Z_j(\eta_j(\theta)), \quad l_j(\theta) = \left\{ [x'_j(\theta)]^2 + [y'_j(\theta)]^2 \right\}^{1/2} \qquad (6)$$

where $x_n(\theta), y_n(\theta)$ are coordinates of some point q at the contour L_n, and $l_n(\theta)$ is an arc length at the point q. We thus obtain the system of N integral equations:

$$\sum_{j=1}^{N} \int_{-\pi}^{\pi} G(R_{sj}(\theta, \tau)) z_j(\tau)d\tau = V_s(\theta), \quad s = 1, \ldots, N \qquad (7)$$

where $R_{sj}(\theta, \tau)$ denotes the distance between some point θ on the s-th boundary and a point τ on the j-th boundary.

Providing that $s \neq j$, the points corresponding to θ and τ belong to the different contours so that $R_{sj}(\theta, \tau) \neq 0$ everywhere and the kernel containing $G(R_{sj}(\theta, \tau))$ is nonsingular; hence, the corresponding integral terms do not contain singularities. For $G_{ss}(\theta, \tau)$ the corresponding integral term contains a singularity of the logarithmic type at the points $\theta = \tau$. In this case, we analytically split the Green's function into a singular part and a regular part L^{sj} that does not contain any singularity:

$$
\begin{aligned}
&-2\pi G(R_{sj}(\theta, \tau)) \\
&= \log(R_{sj}(\theta, \tau)) = L^{sj}(\theta, \tau), \qquad\qquad\qquad s \neq j, \\
&-2\pi G(R_{sj}(\theta, \tau)) \\
&= \log(R_{sj}(\theta, \tau) = L^{sj}(\theta, \tau) + \log\left(2\sin\left| \frac{\theta - \tau}{2} \right| \right), \quad s = j, \quad (8)
\end{aligned}
$$

or equivalently,

$$L^{sj}(\theta, \tau) = \log\left(R_{sj}(\theta, \tau)\right), \qquad\qquad s \neq j,$$

$$L^{sj}(\theta, \tau) = \log\left(R_{sj}(\theta, \tau)\right) - \log\left(2\sin\left|\frac{\theta - \tau}{2}\right|\right), \quad s = j. \qquad (9)$$

The function $L^{sj}, s = j$ is a regular function, defined everywhere except at the points $\theta = \tau$; the function $L^{sj}, s \neq j$ is defined everywhere. The exact expression for $L^{sj}, s = j$ at the points of singularity where $\theta = \tau$ was obtained analytically:

$$L^{sj}(\theta, \tau) = \log\left(l_s(\theta)\right). \qquad (10)$$

We can now extend the definition of the function L^{sj}, $s = j$ everywhere by the formula:

$$L^{sj} = \begin{cases} \log\left(R_{sj}(\theta, \tau)\right) - \log\left(2\sin\left|\frac{\theta-\tau}{2}\right|\right), & \theta \neq \tau, \\ \log\left(l_s(\theta)\right) & \theta = \tau. \end{cases} \qquad (11)$$

This function is continuously differentiable with respect to τ.

We apply a Fourier expansion for the singular part of the Green's function:

$$\log\left(2\sin\left|\frac{\theta - \tau|}{2}\right|\right) = \frac{1}{2}\sum_{\substack{n=-\infty \\ n \neq 0}}^{\infty} \frac{e^{in(\theta-\tau)}}{|n|}. \qquad (12)$$

As the function L^{sj} is regular, we can expand it into a double Fourier series:

$$L^{sj}(\theta, \tau) = \sum_{n=-\infty}^{\infty}\sum_{m=-\infty}^{\infty} l_{nm}^{sj} e^{i(n\theta+m\tau)}. \qquad (13)$$

In a general case, where V_m is a function depending on a position of the point θ on the m-th boundary, we expand it and the unknown function z_j into a Fourier series numerically:

$$-2V_m(\theta) = \sum_{s=-\infty}^{\infty} \nu_s^m e^{is\theta}. \qquad (14)$$

$$z_j(\tau) = \sum_{n=-\infty}^{\infty} \xi_n^j e^{in\tau}. \qquad (15)$$

After substitution of expansions (12)–(15) into (7) we arrive at the system of N integral equations:

$$\sum_{\substack{s=-\infty \\ s\neq 0}}^{\infty} \frac{\xi_s^m}{|s|} e^{is\theta} - 2\sum_{n=1}^{N}\sum_{j=-\infty}^{\infty} e^{ij\theta} \sum_{p=-\infty}^{\infty} \xi_p^n l_{j,-p}^{m,n} = \sum_{s=-\infty}^{\infty} \nu_s^m e^{is\theta}, \qquad (16)$$

where $m = 1, \ldots, N$ and $\theta \in [-\pi, \pi]$. Using orthogonal properties and completeness of the system of functions $\left\{e^{in\phi}\right\}_{n=-\infty}^{n=\infty}$ we obtain an infinite system of algebraic equations, still of the first kind. Now to ensure that matrix coefficients in the resulting system converge with the same rate of convergence and fast enough for the system to be of a second kind we rescale the unknown Fourier coefficients of the charge density function ξ_n^s as:

$$\tilde{\xi}_n^s = \frac{\xi_n^s}{\sigma_n},$$

where $\sigma_n = |n|^{1/2}$, when $n \neq 0$ and $\sigma_0 = 1$. We obtain the following result:

$$\tilde{\xi}_n^s(1 - \delta_{n0}) + \sum_{j=1}^{N} \sum_{m=-\infty}^{\infty} \sigma_n \sigma_m l_{n,-m}^{sj} \tilde{\xi}_m^j = \sigma_n \nu_n^s, \qquad (17)$$

$$n = 0, \pm 1, \pm 2, \ldots; \quad s = 1, 2, \ldots, N.$$

It can be shown that the coefficients of the left-hand side matrix in (17) are square summable and the matrix operator is compact and the system is of a second kind. Thus, the infinite system can be effectively solved by a truncation method. The solution of the truncated system rapidly converges to the exact solution. The above solution automatically incorporates the mutual interaction of all N charged cylinders, allowing accurate calculation of the line charge densities on the boundaries and the field potentials at any point of the space between the conductors.

Due to its theoretical properties the infinite system (17) can be effectively solved for $\tilde{\xi}_m^j$. The linear charge density functions Z are then easily restored from their Fourier coefficients and are used to calculate the capacitance of the system.

3. NUMERICAL RESULTS

The numerical code was validated by comparing obtained results with known analytical solutions for the coaxial line with a centred inner conductor [15] and the coaxial line with a shifted inner conductor [16]. Obtained results entirely coincide with the published solutions starting with $N_{tr} = 16$ for the centred inner conductor and $N_{tr} = 128$ for the inner conductor located close to the shield. It is worth noting that our results are much more accurate than values obtained by the purely numerical method presented in [7]. Their algorithm provides the capacitance value in the centered inner conductor case that is accurate only to two decimal places.
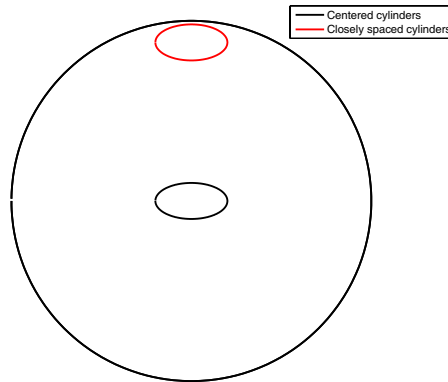
Figure 1. A sample structure for calculation of truncation error.

The efficiency of our algorithm is further demonstrated by computing relative error and condition number dependence on truncation number (Fig. 2) for the structure consisting of an elliptical cylinder with minor and major semi-axes 0.1 and 0.2 correspondingly. The cylinder is placed inside the inner shield of a circular cross-section with radius 1. Two positions of the inner cylinder are considered (Fig. 1): centered (black line) and almost touching the shield (red line). In the numerical code the number of points, used to parameterize each object is set to be equal to the truncation number. For this reason in the case of closely spaced conductors more equations need to be solved (this corresponds to a higher truncation number and more precise parametrization of the curves) to obtain a specific accuracy as can be observed in Fig. 2(a). However, any accuracy can be achieved and solutions are very stable, as demonstrated by condition numbers of the solution matrix in Fig. 2(b).

In our further calculations, we employ the geometry of the 2-D capacitance microscope with a structure similar to the one described in [7]. A scheme of the cross-section of the probe with an object of irregular geometry is shown in Fig. 3. The cross-section of the probe is basically circular, except for the insertion of a small wedge-shaped piece. The wedge-shaped tip is placed at different angular positions (ϕ_p) relative to the object to obtain the image. At each relative position of the probe and the object we determine the capacitance per unit length as a function of ϕ_p. In our calculations we used $N_{tr} = 256$ and 200 steps for each capacitance image. The fast Fourier transform was applied to compute the coefficients in the final matrix equation, resulting in fast calculations. Calculation of each capacitance image took around 6 minutes on a standard computer,
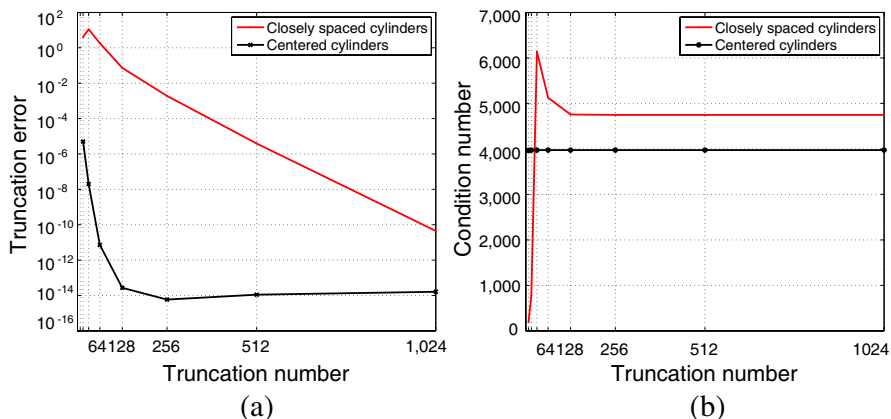
(a)   (b)

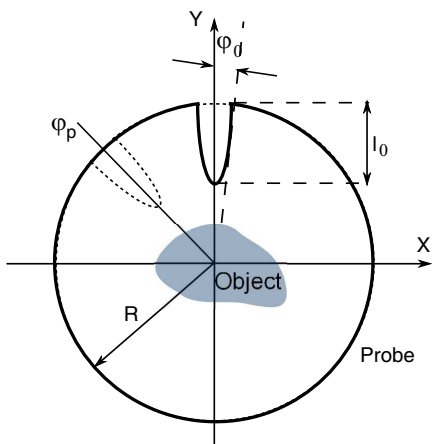**Figure 2.** Relative error and condition number versus truncation number.

Figure 3. Schematic representation of the system probe-object.
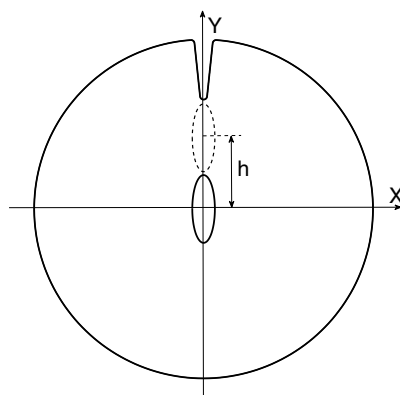

Figure 4. Schematic view of the system with a fixed probe and elevated and rotating sample.

corresponding to less 2 to seconds for each problem involving a single relative object/probe position. The computational time depends on the number of equations solved, and increases with the required accuracy (and thus the truncation number) and with a number of conductors in the system (for the applications other than SCM).

Here a super ellipse Equation (18) is used to parameterize a sample inside the shield and a special parametrization was developed

to describe shield with the probe.

$$\rho(\phi) = \left(\left[\left| \frac{1}{a} \cos \left(\phi \frac{m}{4} \right) \right|^{n_2} + \left| \frac{1}{b} \sin \left(\phi \frac{m}{4} \right) \right|^{n_3} \right]^{1/n_1} \right)^{-1}. \quad (18)$$

In this equation, a and b are the figure size parameters normalized by a biggest cylinder radius R_{char}, n_1, n_2, n_3 define corner sharpness and m represents the symmetry. This formula allows us to model a great variety of smooth shapes such as an ellipse ($n = n_1 = n_2 = n_3 = 2$, $m = 4$), a rectangle with rounded-off corners ($n = n_1 = n_2 = n_3 > 2$, $m = 4$), a star with the smooth rays ($n_1 = 2$; $n_2 = n_3 > 2$, m is equal to the number of rays) and many others.

The wedge-shaped tip on the cylindrical shield (Fig. 3) is parameterized by the two straight lines joined by a part of the circle. The lines are connected to the shield with the similar quarters of the circle. The geometry of the tip is described by the following parameters: l_0 is its length, r_0 denotes a radius of the cylindrical closure between the straight lines, ϕ_0 is the angular measure of such wedge (see Fig. 3). The sensitivity of this method depends on the sharpness of the tip, so we set the angle between the straight lines to be $\phi_0 = \pi/30$. Other geometrical parameters are $l_0 = R/3$, $r_0 = R/48$, where R is a radius of the shield. If the object is described by some planar parametric curve $\rho(\phi)$ with maximum radius $R_0 = \max(\rho(\phi))$, we should require the fulfillment of the condition $\Delta = R - R_0 - l_0 - r_0 > 0$, where Δ is a minimum gap between the object and the wedge-shaped tip. When object's maximum size R_0 is small compared to the radius of the probe ($R_0 \ll R$), it is reasonable to elevate the object from the centre position up to the tip as shown in Fig. 4.

In this case, the only way to preserve a high scanning resolution is to substitute the rotation of the probe by the rotation of the object itself. This rotation is described by the azimuthal angle ϕ'.

To test the sensitivity of the probe in the scanning mode (a sample is centred at the origin) and in the "elevated" mode (the sample is elevated to h) we choose an elliptic cylinder as the sample. Setting $R = 1$, let us define the major semi-axis of the ellipse $b = 0.35$ and the aspect ratio $a/b = 1/4$, where a is the minor semi-axis of the ellipse. The effect of the height of elevation is examined at three successive values: $h = 0$ (SCM), and $h = 0.25, 0.28$ (elevated and rotated sample). When $h = 0.25$, the minimum gap between the wedge-shaped tip and the ellipse is $\Delta = 0.067$; when $h = 0.28$, $\Delta = 0.037$. The graphs of the dimensionless capacitance $C = C_{abs}/(\epsilon_0 R_{char})$ dependence on the rotation angle are shown in Fig. 5.

For the centred sample the dependence $C(\phi)$ (black line) is almost a constant, just slightly exceeding the average level of the capacitance
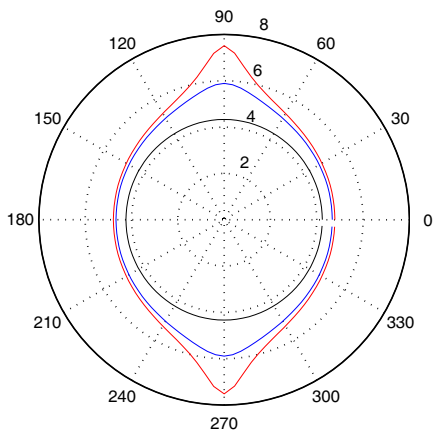
Figure 5. Capacitance versus rotation angle. Sample is the elliptical cylinder with the aspect ratio $a/b = 1/4$. Elevation height: $h = 0$ (black); $h = 0.25$ (blue); $h = 0.28$ (red).
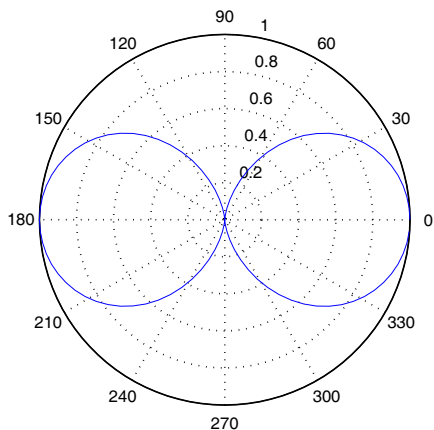

Figure 6. Normalized relative capacitance function $C_{rel}(\phi)$: sample is an elliptical cylinder with the aspect ratio $a/b = 1/4$ ($b = 0.35$); $h = 0$.
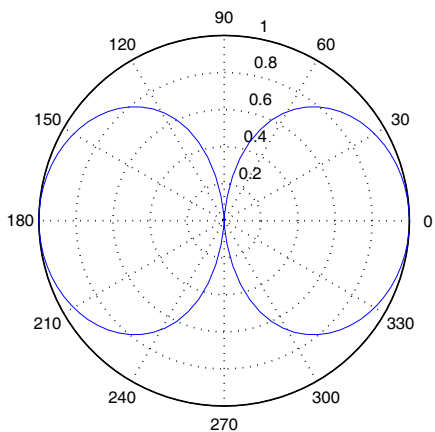

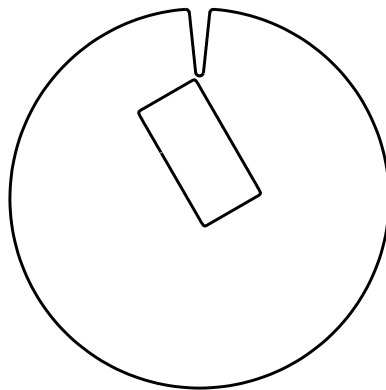**Figure 7.** Normalized relative capacitance function $C_{rel}(\phi')$: sample is an elliptical cylinder with the aspect ratio $a/b = 1/4$ ($b = 0.35$); $h = 0.25$.

Figure 8. Sample: rectangular cylinder with the sides 0.175×0.35.

when the sample passes the tip at the minimum distance $\Delta = 0.037$
($\phi = 90°, 270°$). The minimum capacitance corresponds to the
maximum gap $\Delta = 0.580$ ($\phi = 0°, 180°$). The elevation of the sample
(blue and red lines) leads to the lessening of the gap and hence to the
increase of the capacitance changes.

Scanning the sample by the rotating probe ($h = 0$) or rotating the
sample ($0 < h < R - R_0 - l - r_0$) we obtain the dependence $C(\phi)$. It is
also useful to analyse the normalized relative capacitance behaviour,
which we define as

$$C_{rel} = \frac{\max\left(C(\phi)\right) - C(\phi)}{\max\left(C(\phi)\right)}$$

We plot $C_{rel}(\phi)$ for the two cases: 1) the elliptic sample is positioned
at the centre of the probe ($h = 0$, Fig. 6); 2) elliptic sample is elevated
($h = 0.25$, Fig. 7).

The capacitance graph (Fig. 5) gives very rough estimation of the
object shape, while normalized capacitance behaviour (Figs. 6 and 7)
emphasizes a number of protuberances.

Along with the ellipse, we consider three more complicated
geometries of the sample: a) rectangular cylinder with the
sides 0.175×0.35 (Fig. 8); b) four-ray star-shaped cylinder
(Fig. 12, $a = b = 0.62, n_1 = 2, n_2 = n_3 = 13, m = 4$); c) "rough" or periodically perforated cylinder (Fig. 16,
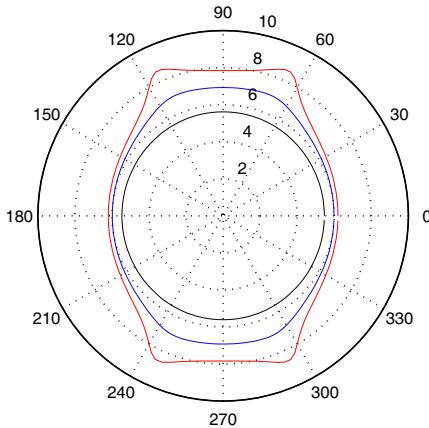$a = b = 0.32, n_1 = 2, n_2 = n_3 = 2.2, m = 20$).

Figure 9. Capacitance versus
rotation angle of the rectangle.
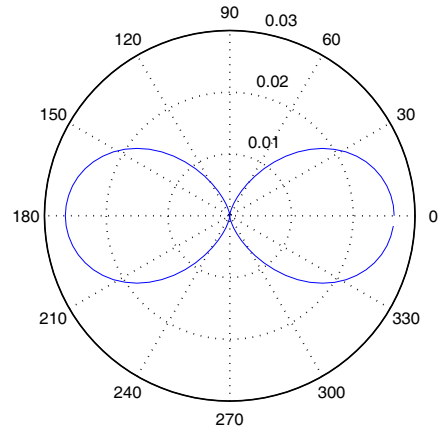Elevation height: $h = 0$ (black);
$h = 0.2$ (blue); $h = 0.24$ (red).

Figure 10. Normalized relative
capacitance function $C_{rel}(\phi_p)$ of
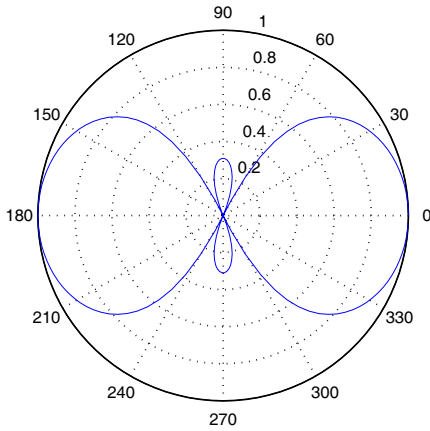the rectangle cylinder, $h = 0$.

Figure 11. Normalized relative capacitance function $C_{rel}(\phi')$ of the rectangle cylinder, $h = 0.24$.
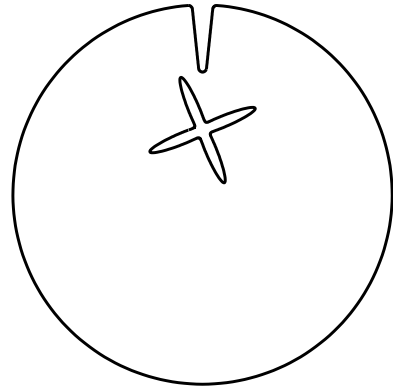

Figure 12. Sample: four-ray star-shaped cylinder ($a = b = 0.62$, $n_1 = 2$, $n_2 = n_3 = 13$, $m = 4$).
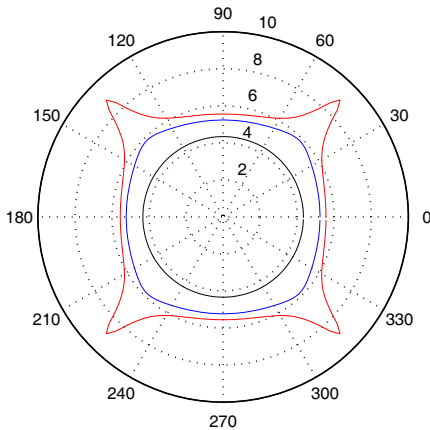

Figure 13. Capacitance versus rotation angle of the star-shaped cylinder.. Elevation height: $h = 0$ (black); $h = 0.3$ (blue); $h = 0.34$ (red).
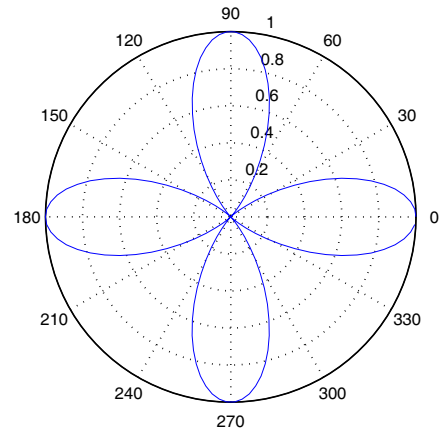

Figure 14. Normalized relative capacitance function $C_{rel}(\phi_p)$ of the star-shaped cylinder, $h = 0$.

The capacitance dependence on the rotation angle graphs for the rectangle shape is shown in Fig. 9. Fig. 10 shows the normalized relative capacitance as a function of the probe rotation angle for
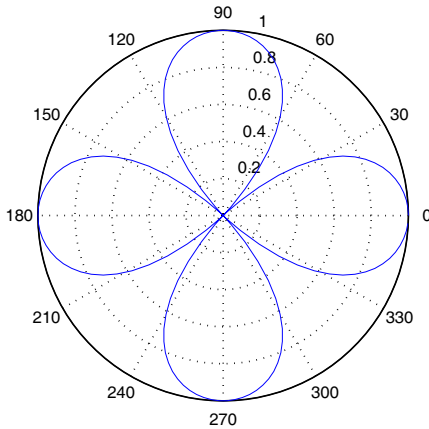
Figure 15. Normalized relative capacitance function $C_{rel}(\phi')$ of the star-shaped cylinder, $h = 0.34$.
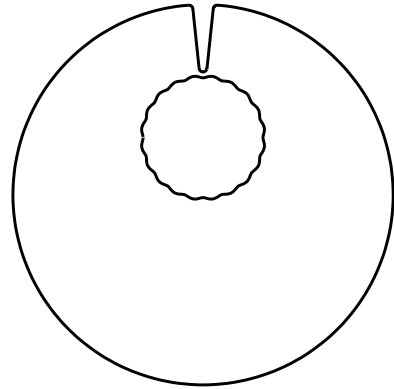
Figure 16. Sample: periodically perforated cylinder ($a = b = 0.35$, $n_1 = 2$, $n_2 = n_3 = 2.2$, $m = 20$).

centrally located sample, and Fig. 11 shows the normalized relative capacitance as a function of the object rotation angle for the elevated sample. It is clear that the closer is object to the probe, the more information we can get from the capacitance image. The red line in Fig. 9, corresponding to the most elevated position of the inner conductor, gives the best estimate of the object shape, and Fig. 11, representing elevated position, gives us correct information on number of protuberances (unlike Fig. 10, representing centered position). The fact that two petals are larger than two others indicates that the corners of the object are not equidistant.

Now we present the similar capacitance and normalized capacitance graphs the various positions of star-shaped cylinder (Figs. 13, 14, 15) and periodically perforated object (Figs. 16, 18, 19).

The calculations of the capacitance in the probe-sample system demonstrate the reliability of the applied method in the investigation of the topography of the metallic samples. The most illustrative results were obtained when the "rough" body case was investigated. Fig. 19 indicates the number of shape protuberances (20), and Fig. 17 clearly reveals the shape itself. These results were most informative because of the very close positioning of the sample near the wedge-shaped tip.
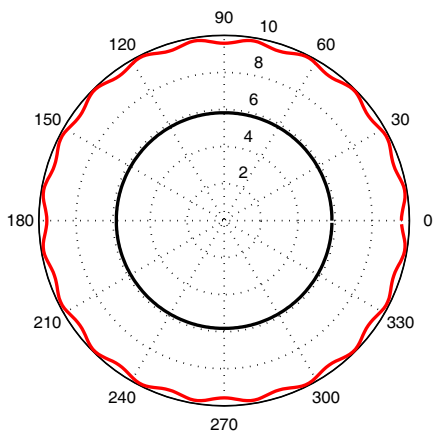
Figure 17. Capacitance versus rotation angle of the periodically perforated cylinder. Elevation height: $h = 0$ (black); $h = 0.3$ (red).
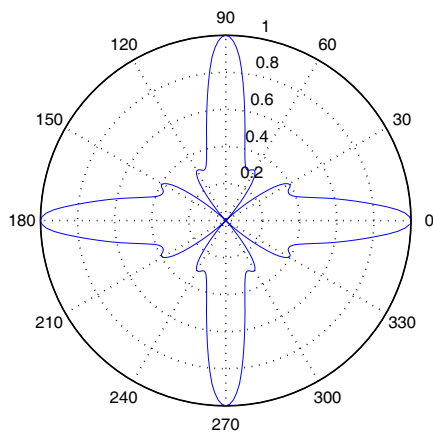

Figure 18. Normalized relative capacitance function $C_{rel}(\phi_p)$ of the periodically perforated cylinder, $h = 0$.
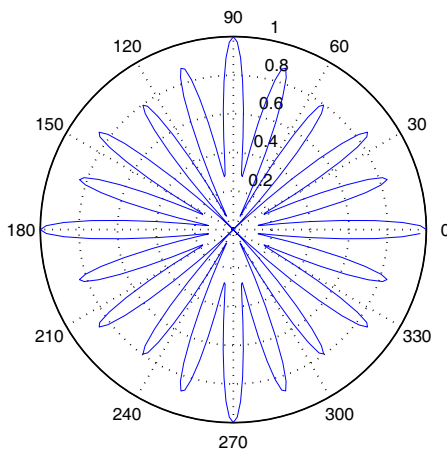

Figure 19. Normalized relative capacitance function $C_{rel}(\phi')$ of the periodically perforated cylinder, $h = 0.3$.

4. CONCLUSIONS

The main point demonstrated in this paper is the proved effectiveness of the developed algorithm in examining the precise details of the probe-sample system geometry and capacitance images. Such images provide useful information about object geometrical parameters.

However, the exact shape of the object cannot be restored. This algorithm can be used as a fast and reliable direct solver required for inverse problem studies, namely for the reconstruction of the shape of an object from the capacitance function $C(\phi)$ or $C_{rel}(\phi)$. The accuracy of the algorithm is ensured by using the method of analytical regularizations and confirmed by truncation error and condition number computations. The small variations of capacitance values (especially for the centred sample and a "rough" body case) confirm the necessity of very high accuracy that can be achieved with the use of our algorithm. The computational code (developed in Matlab) is applicable for the problems with various number of conductors and their shapes. The computational time depends on the number of conductors in the system and the number of equations used; for the two-conductor systems considered above solution for $N_{tr} = 256$ is obtained in less then 2 seconds on a standard computer. Using the results developed for transmission problems in dielectrics [17, 18] our developed method can be generalized on homogeneous and inhomogeneous dielectric samples.

REFERENCES

1. Williams, C. C., "Two-dimensional dopant profiling by scanning capacitance microscopy," *Annual Review of Materials Science*, Vol. 29, 471–504, 1999.

2. Lee, D. T., J. P. Pelz, and B. Bhushan, "Scanning capacitance microscopy for thin film measurement," *Nanotechnology*, Vol. 17, 1484, 2006.

3. Barth, C., T. Hynninen, M. Bieletzki, C. R. Henry, A. S. Foster, F. Esch, and U. Heiz, "AFM tip characterization by Kelvin probe force microscopy," *New J. Phys.*, Vol. 12, 2010.

4. Bocquet, F., L. Nony, and C. Loppacher, "Polarization effects in noncontact atomic force microscopy: A key to model the tip-sample interaction above charged adatoms," *Phys. Rev. B*, Vol. 83, 2011.

5. Sadeghi, A., A. Baratoff, S. A. Ghasemi, S. Goedecker, T. Glatzel, S. Kawai, and E. Meyer, "Multiscale approach for simulations of Kelvin probe force microscopy with atomic resolution," *Phys. Rev. B*, Vol. 86, 2012.

6. Suddards, M., A. Baumgartner, M. Henini, and C. Mellor, "Scanning capacitance imaging of compressible and incompressible quantum Hall effect edge strips," *New J. Phys.*, Vol. 14, 2012.

7. Mendoza-Suarez, A. and F. Villa-Villa, "Integral method for

a capacitance microscope that is based on cylindric metallic surfaces," *Progress In Electromagnetics Research B*, Vol. 21, 203–218, 2010.

8. Wang, C. F., L. W. Li, P. S. Kooi, and M. S. Leong, "Efficient capacitance computation for three-dimensional structures based on adaptive integral method," *Progress In Electromagnetics Research*, Vol. 30, 33–46, 2001.

9. Goharian, M., M. Soleimani, and G. Moran, "A trust region subproblem for 3D electrical impedance tomography inverse problem using experimental data," *Progress In Electromagnetics Research*, Vol. 94, 19–32, 2009.

10. Soleimani, M., C. N. Mitchell, R. Banasiak, R. Wajman, and A. Adler, "Four-dimensional electrical capacitance tomography imaging using experimental data," *Progress In Electromagnetics Research*, Vol. 90, 171–186, 2009.

11. Sacha, G. M., E. Sahagn, and J. J. Saenz, "A method for calculating capacitances and electrostatic forces in atomic force microscopy," *J. Appl. Phys.*, Vol. 101, 2007.

12. Sadeghi, A., A. Baratoff, and S. Goedecker, "Electrostatic interactions with dielectric samples in scanning probe microscopies," *Phys. Rev. B*, Vol. 88, 2013.

13. Vinogradov, S. S., P. D. Smith, and E. D. Vinogradova, *Canonical Problems in Scattering and Potential Theory, Part I: Canonical Structures in Potential Theory*, Chapman & Hall/CRC, 2001.

14. Vinogradov, S. S., P. D. Smith, and E. D. Vinogradova, *Canonical Problems in Scattering and Potential Theory, Part II: Acoustic and Electromagnetic Diffraction by Canonical Structures*, Chapman & Hall/CRC, 2001.

15. Collin, R. F., *Field Theory of Guided Waves*, 2nd Edition, IEEE Press, New York, 1991.

16. Yakover, Y. M., "General analysis of shielded transmission lines with cylindrical geometry conductors," *27th European Microwave Conference*, Vol. 2, 955–958, 1997.

17. Shestopalov, V. P., Yu. A. Tuchkin, A. E. Poedinchuk, and Yu. K. Sirenko, *New Methods of Solving Direct and Inverse Problems of Diffraction Theory*, Osnova, Kharkiv, 1997 (in Russian).

18. Sirenko, Y. K., S. Ström, and J. Chandezon, *Modern Theory of Gratings: Resonant Scattering: Analysis Techniques and Phenomena*, Springer, 2009.